Timing in Thick Silicon Detectors for a Compton Camera

M. Mikuž, A. Studen, V. Cindro, G. Kramberger

Abstract— **In the scope of construction of a PET apparatus based on detection of Compton scattering in silicon (Compton camera), timing properties of 1 mm thick silicon pad and double-sided microstrip detectors are studied. Timing in pad detectors is also investigated for 140.5 keV ^{99m}Tc and 364.5 keV ^{131}I gamma rays in view of a SPECT application. Compton scattering and energy loss of the Compton electron in silicon detector are simulated using the GEANT package. Electric field in the detector is calculated numerically for a fully depleted detector in the abrupt junction approximation, taking into account the geometry and varying the reverse voltage. Signal formation is studied using Ramo's theorem and pulse shaping properties of the trigger circuit. A time-walk cut is seen to be directly corresponding to a deposited-energy cut. At 10 keV threshold in 1 mm thick detectors, 10 ns timing windows are shown to reject a significant portion of events, degrading efficiency or limiting the angular range in a prohibitive way. More involved techniques are therefore suggested, either in the electronics circuit or in later stages of the trigger.**

Keywords— **simulation, Compton camera, PET, SPECT, silicon detectors, charge collection, timing**

I. Introduction

Exploitation of Compton scattering in silicon for electronic collimation of gamma rays emitted from radioactive tracers as a way to improve sensitivity of mechanical collimation used in today's Anger cameras has been around for quite some time [1]. Yet a practical implementation of this tempting principle remains still to be demonstrated, despite substantial efforts of several research groups. The authors are part of a collaboration with Ann Arbor, CERN, Cracow, IDE AS and Valencia [2]. Among the implementations sought, a high-resolution PET Compton camera is the subject of the present study. To obtain sufficient efficiency for 511 keV gamma coincidences, several layers of 1 mm thick double-sided silicon microstrip detectors are envisaged [3]. Coincident detection requires a timing window, which has to be optimized in terms of efficiency versus background rejection. For this purpose, a simulation of detector and trigger electronics response to 511 keV gamma rays has been developed.

A further application of the Compton camera is for specific SPECT examinations [4]. There the smaller size of silicon sensors envisaged permits usage of a pad detector, a solution anyway imposed by the higher rates expected. A narrow timing window in coincident detection of the Compton electron with the scattered photon, detected in a scintillator, is also important here as means to reject background.

Manuscript received December 3, 2001. The authors are with Department of Physics, University of Ljubljana and Jožef Stefan Institute, Jamova 39, SI-1000 Ljubljana, Slovenia (Tel: (+386) 1 4773634, fax: (+386) 1 4257074, e-mail: Marko.Mikuz@ijs.si)

Building a Compton camera is a very complex issue, starting from the many, sometimes conflicting, aspects of design to its materialization in terms of the available and the affordable. This work deals with a limited aspect, that of timing, with no attempt to provide an overview. That will be hopefully available to the interested reader in due time [5]. Also the exact timing requirements are dependent on the specific application, but a value of 10 ns for the timing window is generally regarded as a good benchmark.

II. Basic considerations

Full reconstruction of Compton scattering requires simultaneous detection of the Compton electron in a primary and of the scattered photon in a secondary detector. Using position sensitive silicon detectors for electron detection makes use of their superb position and energy resolution, and the maturity of technology due to developments for high-energy physics applications. Usage of self-triggering fast electronics for silicon read-out provides an additional background rejection tool through coincidences with the scattered photon detector, usually a conventional segmented scintillator ring. In PET, where two photons are emitted, more complex trigger schemes might be thought of [3], but all of them involve fast signals from silicon. Key issues for PET and SPECT differ to some extent. For SPECT, electronic collimation by Compton scattering kinematics, confining the emitted photon direction to a cone, is the driving force. Therefore, energy resolution (ΔE) is as important as spatial, since it results in a spread of the cone angle θ by:

$$\Delta\theta = \Delta E \cdot \frac{(1+\epsilon(1-\cos\theta))^2}{E_\gamma \epsilon \sin\theta}, \qquad (1)$$

with $\epsilon = E_\gamma / m_e c^2$ and E_γ the radio-tracer gamma ray energy. ΔE includes detector resolution. Doppler broadening can also be translated into a θ-dependent energy spread, contributing to ΔE. As an example angular resolutions assuming $\Delta E = 1$ keV FWHM are depicted in Fig. 1 for three typical radio-tracers. Thus, for SPECT, small and large scattering angles or, via Compton scattering kinematics, the respective large and small electron energies, are to be excluded. For PET, various detection schemes might be thought of, but generally no full Compton kinematics reconstruction is envisaged. Secondary photon detectors, although not required in principle, are nevertheless planned. Either just to provide energy constraints to fight background from Compton scattering within the sample, or, in a full-blown version, as a conventional PET scintillator ring to which silicon is an add-on feature, that provides the very high resolution component to the image [3].

Self-triggering is achieved by splitting the input signal and leading one of the signals to a fast shaper and discriminator, providing a sample and hold for the other pulse shaped on a longer time-scale. $CR-RC$ shapers are commonly used, ideally shaping an input signal much shorter than the shaper peaking time τ_p - a "delta-function" pulse - to the form

$$S(t) = A \cdot \frac{t}{\tau_p} \cdot e^{1-\frac{t}{\tau_p}}, \quad (2)$$

with $S(t)$ the shaper output signal dependence on time after input pulse injection at $t = 0$ and A the signal value at its peak at $t = \tau_p$. The discriminator fires at t_0, upon $S(t_0)$ exceeding a threshold value T. An example of signals with $\tau_p = 200$ ns, corresponding to Compton scattered electrons from 511 keV annihilation photons, crossing a 10 keV threshold, is given in Fig. 2.

The time-walk t_0 for large signals ($A \gg T \Rightarrow t_0 \ll \tau_p$) can be derived from (2) as

$$t_0 = \tau_p \cdot \frac{T}{e \cdot A}. \quad (3)$$

For smaller signals, (2) has to be inverted numerically. Fig. 3 shows the time-walk distribution for $\tau_p = 200$ ns and $T = 10$ keV, obtained by generating A according to electron energy distribution in Compton scattering (Klein-Nishina). The $1/A$ dependence in (3) leads to the sharp peak at low t_0 and the long tail toward τ_p is corresponding to low energy deposits in forward scattering.

Obviously a timing window, under such assumptions, directly corresponds to a cut in deposited energy of the scattered electron ($\propto A$) and, by Compton kinematics, to a cut in the scattering angle. The large scattering angles, identified as useless for SPECT in Fig. 1, contribute to a very small time range at small t_0, at the steep edge of the peak. In Fig. 3 it can be seen that all the scatters from ^{99m}Tc photons with $\theta > 120°$ are confined within the first 3 ns. On the other hand, the useful angles get distributed over a broad time-walk range. Setting a timing window of 10 ns, starting from shortest t_0 (backward scattering), cuts away all scatters with $\theta < 40°$ for 511 keV, and even $\theta < 100°$ for 140.5 keV gammas of ^{99m}Tc, the latter certainly not tolerable. Even a more generous 20 ns window still requires $\theta > 75°$ and 40 ns would be needed to extend the angular acceptance down to 60°.

Having identified the extent of the problem, a couple of points deserve further consideration:

1. As the attenuation coefficient for 511 keV γ in Si amounts to $\mu = 0.2$ cm^{-1} only, thick silicon detectors ($w \sim 1$mm) are needed to obtain acceptable detection efficiency in a small number of detector layers. Thus, for affordable reverse biases of $V \sim 500$ V, charge collection times $\tau_c = w^2/(V\mu)$ are of the order of 30 ns for holes due to their lower mobility μ. For 1 mm detectors, full depletion voltage is 300 V even for detectors fabricated on 10 kΩcm Si bulk, so electric field varies considerably through the detector. Due to possible signal generation in the low field region, the signal formation times might get even longer, and the "delta-function" pulse assumption hard to justify.
2. Range of energetic scattered electrons near the Compton edge, especially for high-energy photons from positron annihilation, exceeds 100 μm. Thus part of the electron energy can be escaping detection in silicon and this, according to (3), increases the time-walk.
3. For strip detectors, notably p^+ strips on n bulk, the weighting (Ramo) field is non-uniform, its low values coinciding with the low electric field region. Signal build-up times can thus get even longer, increasing further the time-walk for events where the signal charge is created in these regions.
4. Read-out electronics is not an ideal $CR-RC$ shaper, thus (2) has to be modified accordingly. Noise introduces its own trigger time variation, known as jitter. Jitter can be estimated by

$$\sigma_t = (dS/dt|_{S=T})^{-1} \cdot N, \quad (4)$$

with σ_t the jitter, N the noise variance and dS/dt the signal slope evaluated at the threshold crossing point. For large pulses ($A \gg T$) of form according to (2): $\sigma_t = (S/N)^{-1}\tau_p/e$ is obtained. To compare with time-walk from (3), jitter should be multiplied by 2.35 to get its FWHM and then added in quadrature to the time-walk range to get an overall estimate of timing excursions. For $S/N \approx 10$ thus τ_p of less than 100 ns needs to be used to keep the jitter under the benchmark value of 10 ns.

To study the first three effects, a full Monte Carlo simulation study was conducted, taking into account photon and electron interactions as well as details on signal formation in the detector.

III. Detector set-up

GEANT simulation package is used to configure the detector set-up and to track positrons, gamma rays and secondary Compton electrons and photons. An exploded view of the set-up is shown in Fig. 4. A positron source is placed at the origin, surrounded by a 2 cm diameter cylinder of water, representing tissue. The primary detector consists of 10 layers of silicon detectors. Each of the layers forms an octagonal prism of 8 individual detectors, the first at 3 cm around the source. Size of detectors, 25 mm $\times$ 25 mm, matches the octagon and covers about 40 % of the solid angle. Detector thickness is 1 mm, yielding 511 keV gamma detection efficiency of 2 % per layer. Two types of detectors were considered: pad detectors and double sided strip detectors. Pad detectors have 1.4 mm $\times$ 1.4 mm p^+ pads to match our prototype detectors [2]. Strip detectors feature orthogonal p^+ and n^+ strips on each side of the high resistivity, n-type substrate, running parallel/perpendicular to the symmetry axis of the set-up. Strips are 0.3 mm wide on a 0.4 mm pitch as a compromise to limit in-homogeneities of weighting and electric fields and control the inter-strip capacitance. The silicon detector is surrounded by a scintillator octagonal prism at 10 cm distance. As the emphasis of the study was on timing properties of silicon detectors, details on scintillators were left unspecified and will be updated at a later stage. It was assumed, however, that

scintillators are providing trigger signals of superb timing resolution with respect to signals from silicon detectors.

Many features of this set-up are meant for detailed studies of Compton camera for PET applications, and are certainly an overkill for the present timing study. But having the full-blown simulation available, it was easy to turn off unwanted blocks, so the same set-up was used to investigate timing even for SPECT.

IV. Tracking

Starting from a fixed energy positron, launched in random direction from the origin, all tracking is under control of GEANT. The positron annihilates in water, sending the two 511 keV photons into the apparatus. Alternatively, 140.5 or 364.5 keV photons from a point source at the origin are generated directly. Some of the gamma rays interact in silicon detectors. Details on signal formation, starting from energy deposition of the Compton scattered (or, to a minor extent, resulting from photo-electric effect) electron through ionization in silicon, to induced currents resulting from drift of the generated charge in the electric field of the detector are the key issues to understand timing properties.

The pad detector is treated as a one-dimensional object, the only relevant coordinate along its depth, perpendicular to the pads. The detector is divided into 1000 1 μm thick layers, and the deposited energy recorded in each of them. While providing an insight into gross features of the timing, we are ignoring the division into pads of dimensions that are of the same order of magnitude as the detector thickness (1.4 mm vs. 1 mm). This results in an underestimate of the time-walk, mainly due to in-homogeneities of the weighting field near the pad edges. But the proper approach would involve a full 3-dimensional analysis and was well beyond the scope of this study. The double-sided detector is factorized into two single-sided detectors, ignoring the division into strips on the other side, thus reducing the problem to two dimensions. Each detector strip is divided into 16×40 square ($25\ \mu\text{m} \times 25\ \mu\text{m}$) cells along its width/thickness. Separate orthogonal cell divisions are maintained for each detector side, the deposited energy per cell recorded and passed over to signal processing. As photon energy depositions are uncorrelated, all the signals from individual photons are taken and no attempt to form coincidences or to track photons to scintillators is made in this simulation exercise.

To connect to existing measurements [2], time response of the pad detector to electrons from a ^{90}Sr β^- source was also simulated, closely emulating the test set-up. The β^- electrons were required to cross the silicon detector at an angle of less than 10 degrees and to reach a scintillator at 8 cm from the silicon. Electrons need $T_e > 1$ MeV to penetrate the 1 mm of silicon, and their energy deposition thus resembles that of a minimum ionizing particle. Energy deposited along their path in the 1000 layers of the silicon detector was recorded as in the case of photon signals.

V. Signal formation

The energy deposited in individual cells (or layers) is converted into electron-hole pairs at 3.6 eV for each pair. Time starts running upon creation of pairs, possibly neglecting application-dependent time-of-flights of nanosecond order. Normalized current shapes $i^{i,j}_{e,h}(t)$ for electrons and holes for each cell (i,j) are pre-stored in a look-up table. They were obtained by applying Ramo's theorem [6]

$$i_{e,h}(t) \;=\; q\vec{E}_w(\vec{r}_{e,h}(t))\,\mu_{e,h}\,\vec{E}(\vec{r}_{e,h}(t)) \tag{5}$$

to a unit charge created at the centre of cell (i,j) at $t = 0$ and moving under the influence of electric field $\vec{E}$ to the electrode with weighting (Ramo) field $\vec{E}_w$. The time-dependence of the position of the moving charges $\vec{r}_{e,h}(t)$ is obtained by solving the equation of motion in the electric field of the detector:

$$\frac{d\vec{r}_{e,h}}{dt} = \vec{v}_{e,h}(t) = \mu_{e,h}\,\vec{E}(\vec{r}_{e,h}(t)). \tag{6}$$

For the pad detector, weighting field was approximated as uniform, $E_w = 1/w$ (w - detector thickness), reducing the problem to one dimension. The electric field for a $p^+{-}n$ pad detector in the abrupt junction approximation is linear:

$$E = \frac{2V_{FD}}{w^2}\cdot x + \frac{V - V_{FD}}{w}, \tag{7}$$

for reverse biases V above the full depletion voltage V_{FD}. The coordinate x is running from the back-plane to the p^+ pad. For strip detectors, weighting field was obtained by numerically solving the two-dimensional Laplace equation of an array of strip electrodes against a back-plane electrode, with all of them grounded, except for the sensing one being at unit potential. Electric field calculation involved solving the Poisson equation, using a homogeneous positive space charge distribution in the silicon volume with a fixed potential difference between the strips and the detector back-plane that was exceeding the full depletion voltage (see [7] for details). Both solutions were obtained on a 4 μm mesh over the volume of 3 adjacent strips. The boundary conditions were defined either by the electrodes' potential or by demanding no electric field perpendicular to the boundary surface. An example of the resulting electric field for a detector produced on a 15 kΩcm substrate reverse-biased to 500 V ($V_{FD} = 230$ V) is shown in Fig. 5.

There is an important distinction between signals induced on the p^+-strips vs. those on the n^+ side. For the former, high weighting field next to the strip coincides with the high electric field region, while for n^+-strips the electric field is higher on the far side. This is best illustrated by plotting the dot product $\vec{E}_w \cdot \vec{E}(x,y)$, directly proportional to the current signal. From Fig. 6 it can be deduced, that signals induced by interactions far from the strips build up faster on n^+ than on p^+-strips. This effect gets amplified by the larger mobility of electrons, drifting to n^+ strips with respect to holes, directed to p^+ strips.

The total induced current for each side is obtained by summing over the electron and hole currents of individual

cells of the respective strip. Only strips under which there was an energy deposition are taken into account, as the bipolar current pulses on adjacent strips turn out negligible in most of the cases.

VI. Trigger conditions

Simulation of the trigger follows closely the trigger circuit of the TA trigger chip, developed by IDE AS, Norway [8]. The TA is fed off the VA pre-amplifier, which can be in this case treated as a perfect integrator, with $V_{out}(t) = 1/C \int i(t)dt$. The VA path then uses a slow (few μs) shaper to accurately measure the signal amplitude. TA includes a $CR-RC$ shaper circuit with a peaking time of 200 ns, followed by a discriminator, firing at the leading edge of signal exceeding an adjustable threshold. The peaking time is a compromise of two conflicting requirements: timing would profit from shorter rise-times, while noise, dominated by voltage noise at such short τ_p, increases as $1/\sqrt{\tau_p}$. The RMS noise of the TA corresponds to an input charge of about 300 electrons or about 1 keV energy loss in silicon. The induced current signal from the detector is integrated and then shaped numerically with a $CR-RC$ filter with 200 ns peaking time. The time when the signal (if ever) crosses the threshold is recorded. For our study, the threshold was set at 10 keV, as TA operation at lower thresholds proved unstable [2]. Both noise and threshold are given as input charge equivalents, that would result from signals with collection times much shorter than τ_p. The resulting $S/N > 10$ should keep the jitter contribution small and suppress the noise trigger rate to a negligible level. Lowering the threshold, if feasible in future versions of the read-out chip, is certainly advantageous in terms of time-walk and acceptance of small Compton scattering angles, especially for ^{99m}Tc. On the other hand, one should be cautious of the noise-induced trigger rate R_n given in terms of the threshold to noise ratio T/N by [9]

$$R_n = \frac{1}{4\sqrt{3}\tau_p} \cdot e^{-\frac{1}{2}(T/N)^2}. \qquad (8)$$

Both lower thresholds and shorter τ_p ultimately provoke R_n that could become unacceptable in a system with many read-out channels.

VII. Results

Let us begin with ^{90}Sr results in Fig. 7. The energy deposition in silicon follows a nearly perfect Landau profile, peaking at 350 keV. The pad detector was at 350 V bias, only slightly above V_{FD} of 320 V, matching measured V_{FD} of a prototype pad detector [2]. Even with this highly non-uniform field, the time-walk distribution is very sharp, with a FWHM of 2 ns. Some tail to short times can be observed, correlated to the high energy deposits.

The pad detector exercise is repeated under same conditions for 140.5 keV photons from ^{99m}Tc (Fig. 8), 364.5 keV from ^{131}I (Fig. 9) and 511 keV annihilation gamma rays (Fig. 10). The anticipated, larger time-walk spread with respect to that obtained by simple considerations in Fig. 3 is observed, although the gross features of the distribution, the sharp edge and the long tail, are preserved. The same is true for the correlation; lower bound on the time-walk at each energy deposit corresponds to that for a "delta-function" pulse according to (2). The correlation is well pronounced and could be incorporated into a higher-level trigger decision, combining the timing datum from the TA and the accurate energy deposit information from the VA chip in a DSP unit. Incorporation of pulse height compensation in the electronics, like constant fraction, represents another solution. But following a simple time-walk window requirement, the 10 ns benchmark is passed by 20, 45 and 60 % of events, for 140.5, 364.5 and 511 keV, respectively. While this might appear promising at first sight, one should keep in mind, that at least for ^{99m}Tc most of the events kept result from large-angle scattering and are therefore useless for SPECT. For keeping 70 % of events, time windows of 100, 25 and 17 ns are required. Moving to higher detector biases brings only marginal improvement as seen in Fig. 11 showing time-walk for ^{99m}Tc with the pad detector at a bias of 500 V.

Usage of the double-sided strip detector is envisaged for PET, therefore only its response to 511 keV photons was studied. Bulk of the highest resistivity commercially available was taken in the simulation (15 kΩcm $\Rightarrow V_{FD} = 230$ V for 1 mm thick detectors) and the bias set to the high-end value of 500 V as means to reduce signal non-uniformity. Resulting time-walk, its correlation to energy deposit and detection efficiency versus time-walk window are exhibited in Fig. 12 for the p^+-strip signals and in Fig. 13 for the n^+-strip signals. Long tails to large time-walks for the p^+-strips are a consequence of slow signal build-up by charge created far from the strips. Also the correlation is spoiled, now much less pronounced than for the pad detector. This puts doubts in the merit of pulse-height compensation techniques for a p^+-strip detector. Clear benefits of the more uniform signal on n^+-strips can be observed. FWHM of the time-walk distribution is nearly half of that for p^+-strips, the tail reduced significantly and the correlation preserved. This feeds also into efficiency curves. For a 10 ns time-walk window, n^+-strips are 50 % efficient while the figure for p^+-strips reads 30 % only. To reach 80 % efficiency timing windows of 30 (for n^+) and 45 ns (for p^+)are required. An interesting possibility, offered by the double-sided detector, is to trigger on the coincidence of signals from the two sides. Fig. 14 shows the time-walk difference between the p^+ and n^+-strips. The peak in Fig. 14(a) corresponds to photons interacting in the middle of the detector bulk, while tails contain events with charge produced close to the respective strips. This is valid regardless of the energy deposited (see Fig.14(b)), although the distributions at low energy deposits get substantially broader. 45 % of events are contained within a 10 ns window and 80 % within 30 ns.

The only improvement recognized for strip detectors is in reducing the shaping time of the trigger stage. Setting it to 75 ns (Fig. 15), as was the case in a former TA chip version, yields efficiencies of 45 (p^+), 65 (n^+) and 60 % ($p^+ - n^+$ difference) for a 10 ns timing window. This should

be judged against the increase in noise, possibly requiring a higher threshold.

VIII. Conclusions

Simulation of the response of thick silicon pad and microstrip detectors to Compton scattered gamma rays exhibits interesting, although not always promising, timing features. In pad detectors, it was shown that a time-walk window is directly correlated to a cut in deposited energy. Through Compton kinematics this gets translated into a cut in the scattering angle, a feature to watch for in SPECT applications with low-energy radio-tracers as ^{99m}Tc. Generally, the 10 ns timing benchmark can hardly be met in a straight-forward way. Exploitation of the time-walk – deposited-energy correlation is suggested, either in terms of pulse-height compensation built into the trigger chip or with signal processing in software at a later trigger stage. In a double-sided strip detector, used to detect 511 keV annihilation photons, further degrading of timing is observed due to non-homogeneous charge collection, despite the ultra-pure base material and high bias envisaged for its operation. The degradation is more limited for signals from n^+-strips. An additional timing handle is provided by the coincidence between signals from p^+ and n^+-strips, which is shown to provide good timing features on its own. From the study it is clear that detailed timing schemes are to be worked out for each specific application. Care should be taken, as shaping time and threshold value of the trigger stage, while providing the most direct handle on timing, also influence other parameters, governing the overall performance of a Compton camera imaging system.

References

[1] R.W. Todd, J.M. Nighting, D.B. Everett, *Nature* **251** (1974) 132-134.

[2] D. Meier, A. Czermak, P. Jalocha, B. Sowicki, M. Kowal, W. Dulinski, et al.: "Silicon detector for a Compton camera in nuclear medical imaging," in *IEEE NSS-MIC (2000) Conf. Rec.*, 22-6, CERN-EP 2001-009,
A. Studen, V. Cindro, N. H. Clinthorne, A. Czermak, W. Dulinski, J. Fuster et al.: "Development of silicon pad detectors and readout electronics for a Compton camera," *presented at* 10^{th} *International Workshop on Vertex Detector, Brunnen, September 2001*, submitted to *Nucl. Instr. Meth. A*.

[3] S. Park, L. Han, S.J. Wilderman, P. Sukovic, A. Czermak, P. Jalocha, et al.: "Experimental setup for very high resolution animal PET based on solid state detector," in *IEEE NSS-MIC (2001) Conf. Rec.*, M3-1.

[4] L. Zhang, N.H. Clinthorne, S.J. Wilderman, C. Hua, T.J. Kragh, W.L. Rogers: "An innovative high efficiency and high resolution probe for prostate imaging" (abs), *J. Nucl Med* **41**(5) (2000) 18.

[5] W.L. Rogers, N.H. Clinthorne, A. Bolozdynia: "Compton cameras for nuclear medical imaging", manuscript in preparation, private communication.

[6] S. Ramo, *Proc. IRE* 27 (1939) 584.

[7] G. Kramberger, V. Cindro, M. Mikuž, *Nucl. Instr. Meth.* **A457** (2001) 550-557.

[8] Integrated Detector and Electronics (Ideas ASA), `http://www.ideas.no`, P.O.B. 315, Veritasveien 9, N-1322 Hvik, Norway.

[9] H. Spieler (2001, October): "Radiation detectors and signal processing", *Lectures given at Univ. Heidelberg*, part IV/6, Available: `www-physics.lbl.gov/~spieler/Heidelberg_Notes/` ,
Rice, *Bell Sys. Tech. J.* **23** (1944) 282 and **24** (1945) 46.

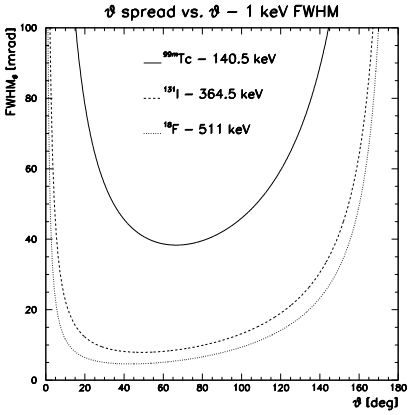

Fig. 1. Scattering angle resolution as a function of scattering angle, assuming a 1 keV electron energy spread, for 140.5 keV photons from ^{99m}Tc, 364.5 keV photons from ^{131}I and 511 keV positron annihilation photons.

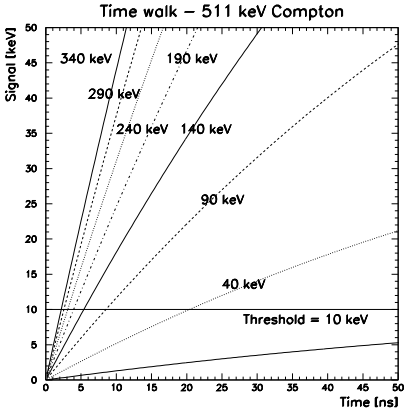

Fig. 2. Examples of signals crossing the 10 keV threshold for various electron energies encountered in Compton scattering of 511 keV positron annihilation photons.

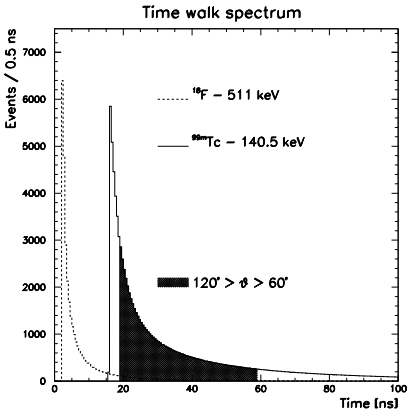

Fig. 3. Toy simulation of time-walk, taking into account Compton energy spectra and ideal 200 ns $CR - RC$ shaping with the discriminator threshold set at 10 keV. Time-walk spectra for 511 keV positron annihilation photons and 140.5 keV photons from ^{99m}Tc, where θ range from 120 to 60° is shown hatched.

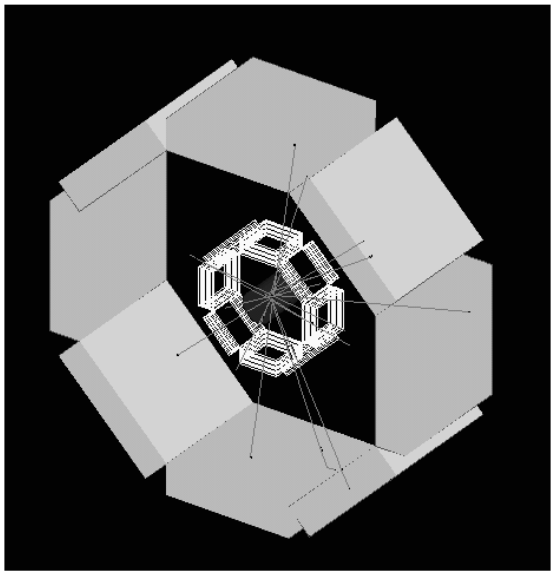

Fig. 4. Simulation set-up. From the centre outwards: water cylinder, stacks of silicon detectors and scintillator octagon.

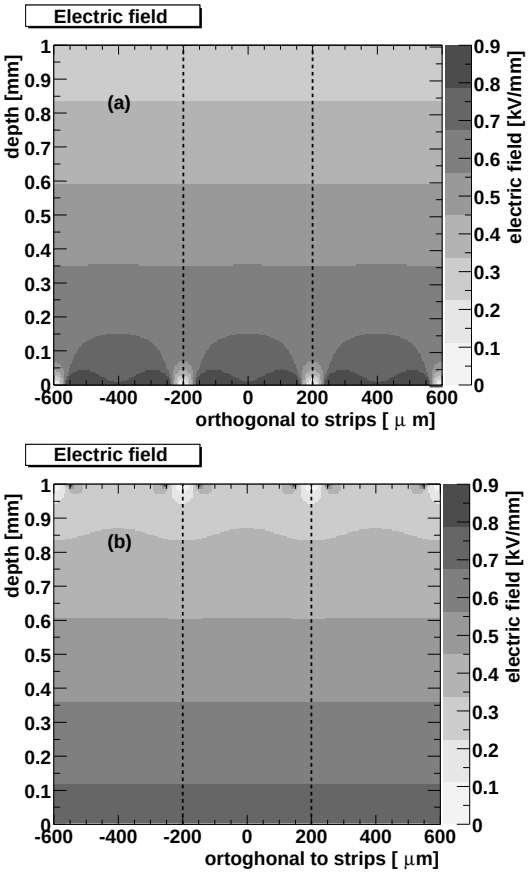

Fig. 5. Calculated electric field in a 1 mm thick double-sided strip (0.4 mm pitch, 0.3 mm wide) detector with $V_{FD} = 230$ V at a bias of 500 V: (a) p^+-strips on bottom and (b) n^+-strips on top.

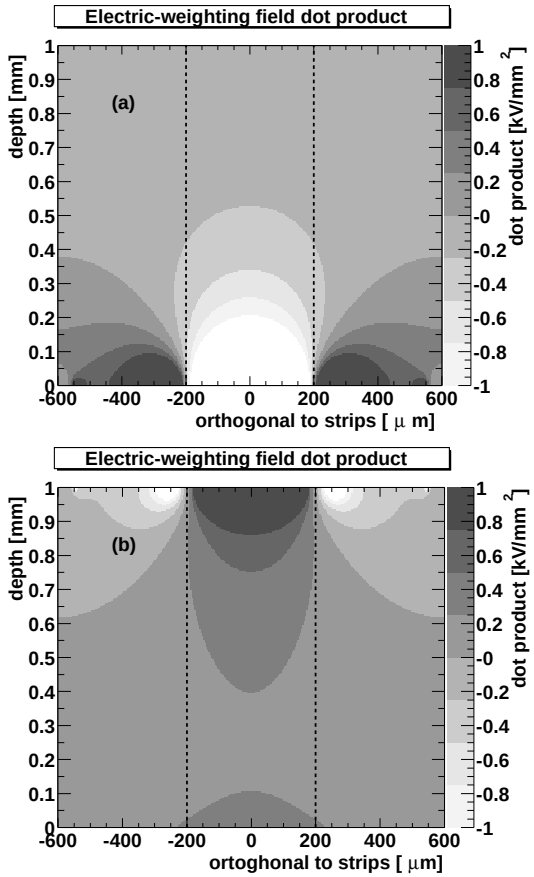

Fig. 6. Dot product of electric and weighting fields in a 1 mm thick double-sided strip detector for: (a) p^+-strips and (b) n^+-strips. Both sets of strips are at 0.4 mm pitch and 0.3 mm wide. Detector with $V_{FD} = 230$ V is at a bias of 500 V. White denotes regions where $\vec{E}_w \cdot \vec{E} < -1$ kV/mm^2.

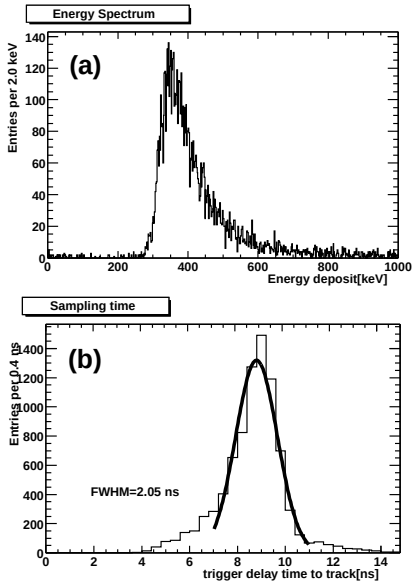

Fig. 7. Timing for electrons from ^{90}Sr in a pad detector: (a) energy deposit in silicon and (b) time-walk distribution.

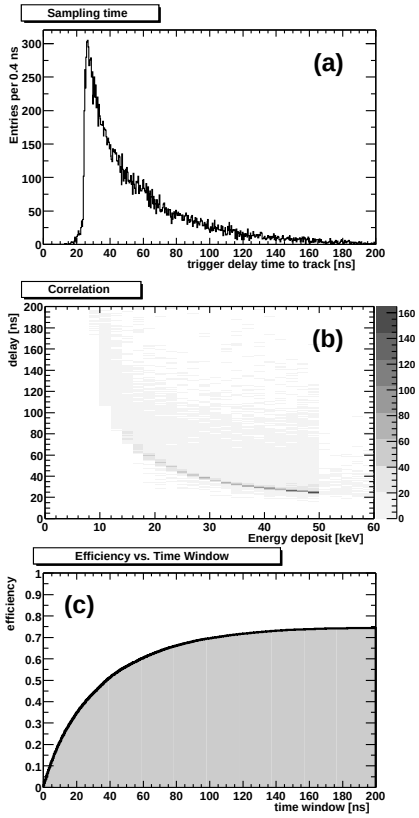

Fig. 8. Timing for 140.5 keV photons from ^{99m}Tc in a pad detector: (a) time-walk distribution, (b) time-walk - energy-deposit correlation and (c) efficiency vs. time window.

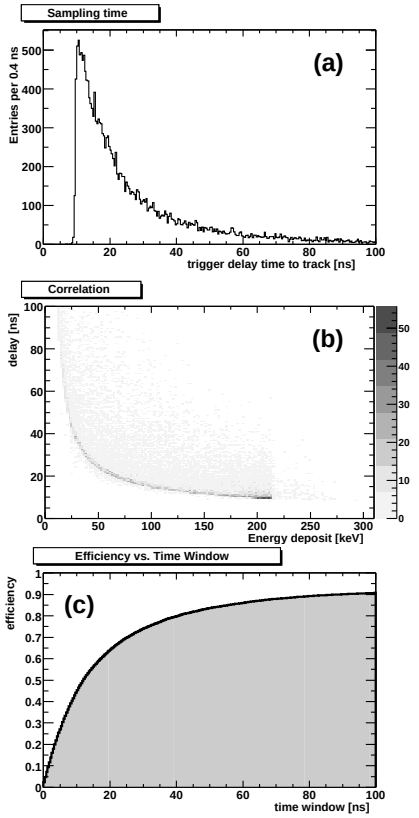

Fig. 9. Timing for 364.5 keV photons from ^{131}I in a pad detector: (a) time-walk distribution, (b) time-walk - energy-deposit correlation and (c) efficiency vs. time window.

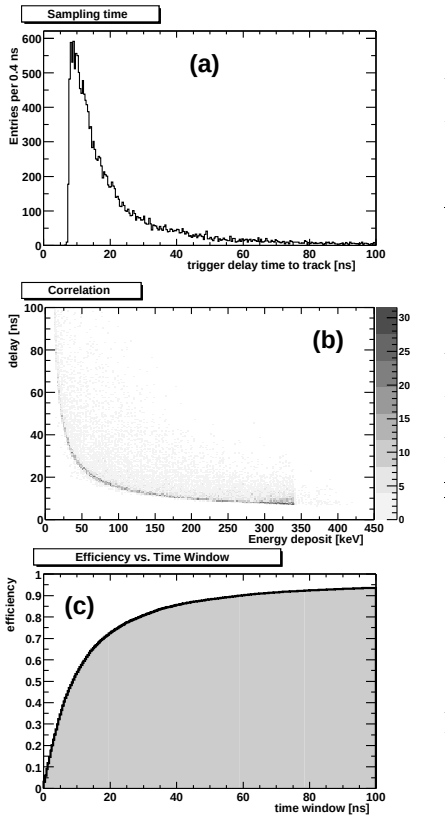

Fig. 10. Timing for 511 keV positron annihilation photons in a pad detector: (a) time-walk distribution, (b) time-walk - energy-deposit correlation and (c) efficiency vs. time window.

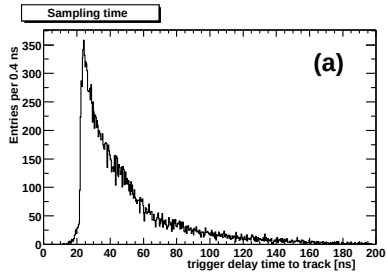

Fig. 11. Time-walk for 140.5 keV photons from ^{99m}Tc in a pad detector at an increased bias of 500 V.

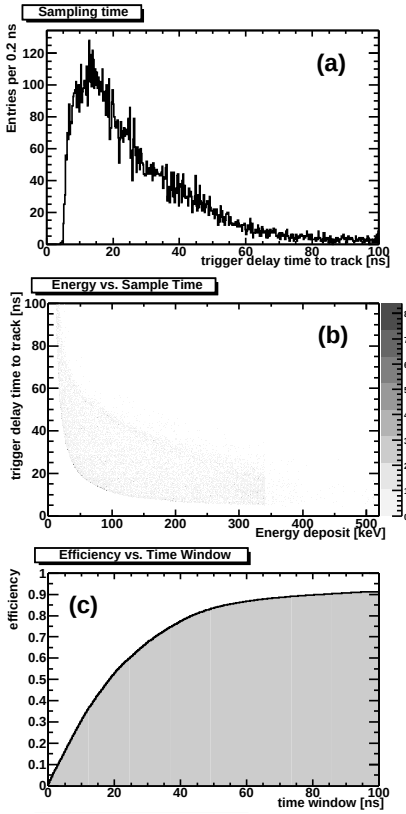

Fig. 12. Timing for p^+-strips of a double-sided detector: (a) time-walk distribution, (b) time-walk - energy-deposit correlation and (c) efficiency vs. time window.

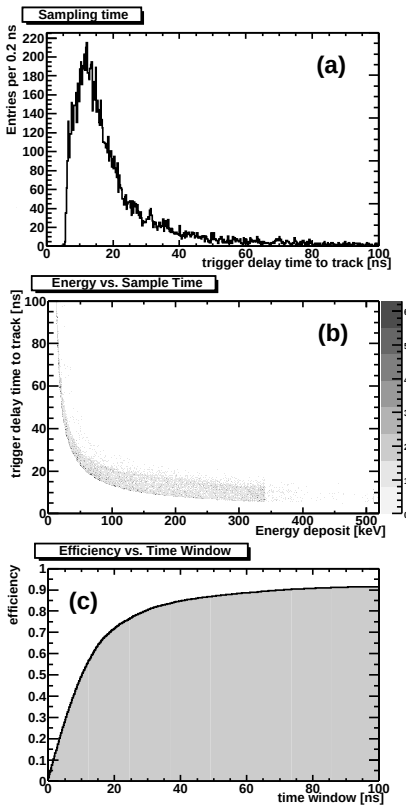

Fig. 13. Timing for n^+-strips of a double-sided detector: (a) time-walk distribution, (b) time-walk - energy-deposit correlation and (c) efficiency vs. time window.

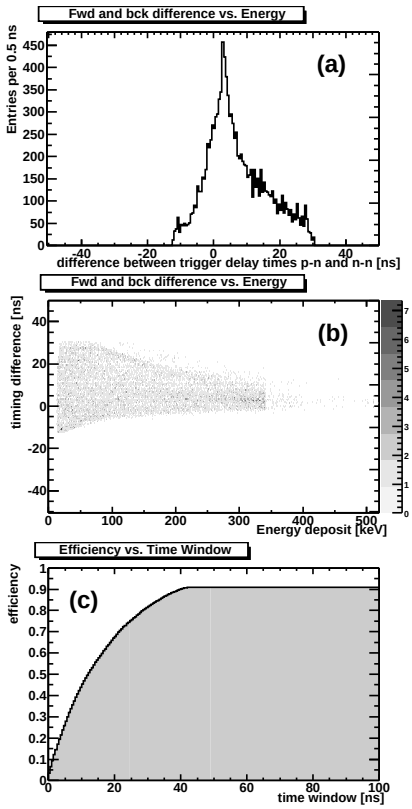

Fig. 14. Trigger time difference between p^+ and n^+ strips of a double-sided detector: (a) time difference distribution, (b) time - energy-deposit correlation and (c) efficiency vs. time window.

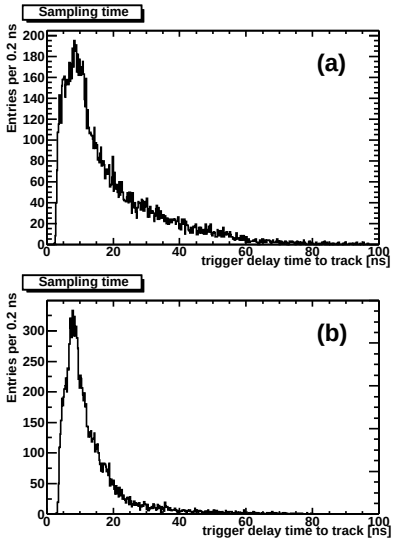

Fig. 15. Time-walk in a double-sided strip detector with reduced shaping time of 75 ns for annihilation photon signals on: (a) p^+-strips and (b) n^+-strips.